



Decreased motivation during chronic pain requires long-term depression in the nucleus accumbens

Neil Schwartz *et al.*

Science **345**, 535 (2014);

DOI: 10.1126/science.1253994

This copy is for your personal, non-commercial use only.

If you wish to distribute this article to others, you can order high-quality copies for your colleagues, clients, or customers by [clicking here](#).

Permission to republish or repurpose articles or portions of articles can be obtained by following the guidelines [here](#).

The following resources related to this article are available online at www.sciencemag.org (this information is current as of August 9, 2014):

Updated information and services, including high-resolution figures, can be found in the online version of this article at:

<http://www.sciencemag.org/content/345/6196/535.full.html>

Supporting Online Material can be found at:

<http://www.sciencemag.org/content/suppl/2014/07/30/345.6196.535.DC1.html>

A list of selected additional articles on the Science Web sites **related to this article** can be found at:

<http://www.sciencemag.org/content/345/6196/535.full.html#related>

This article **cites 54 articles**, 11 of which can be accessed free:

<http://www.sciencemag.org/content/345/6196/535.full.html#ref-list-1>

This article has been **cited by** 1 articles hosted by HighWire Press; see:

<http://www.sciencemag.org/content/345/6196/535.full.html#related-urls>

This article appears in the following **subject collections**:

Neuroscience

<http://www.sciencemag.org/cgi/collection/neuroscience>

decoherence by applying an XY4 dynamical decoupling sequence (19, 28, 29). The time between entanglement generation and the triggering of the feed-forward operation based on the BSM outcome is 300 μ s. For this duration, the decoupling protocol preserves the qubit state, with an average fidelity of 0.96 ± 0.02 .

Verifying quantum teleportation

We first verify that the teleporter is calibrated correctly by applying it to the nominal input state $|Y\rangle = (|0\rangle + i|1\rangle)/\sqrt{2}$ and performing tomography on the state that appears on Bob's side. The reconstructed density matrix (Fig. 4B) shows that the target state vector is aligned well with Y and therefore that the reference frames of Alice and Bob are correctly set.

To prove that our quantum teleporter outperforms any classical communication strategy, we teleport an unbiased set of six basis states $|\psi\rangle$ (Fig. 4A) and determine the fidelity of the teleported state on Bob's side with respect to the ideal input state. In these experiments, we use a feed-forward operation that maps the ideal state of qubit 3 onto a qubit eigenstate such that the readout directly yields the teleportation fidelity (23). Because the feed-forward operation is conditional on the BSM outcome, ignoring the BSM outcome yields a completely mixed state and random outcomes, ensuring that no information is transmitted. Without feed-forward, we indeed observe a mean teleportation fidelity, averaged over all six input states, of $\langle F \rangle = 0.50 \pm 0.03$ (Fig. 4C). In contrast, including the feed-forward loop, we find that $\langle F \rangle = 0.77 \pm 0.03$. This value exceeds the classical limit of $2/3$ by more than 3 standard deviations, thus proving the quantum nature of our teleporter (30). We note that this fidelity presents a lower bound on the actual teleportation fidelity because it does not take into account initialization errors of the source state. Notably, this result is obtained without any postselection: Each teleportation attempt is included in the data presented here.

We also simulate the outcomes by using independently determined infidelities in the protocol. The only unknown parameter is the fidelity of the entangled state shared by Alice and Bob. We find that our data are well reproduced by the simulations if we assume a fidelity to the ideal Bell state $|\Psi^-\rangle_{23}$ of 0.87 (Fig. 4C). The simulations also enable us to quantify the effect of imperfect initialization of the source qubit on the measured fidelities. In this way, we estimate the teleportation fidelity to be ~ 0.86 (23).

Conclusions and outlook

The ability to generate remote entanglement and to control and read out multiple qubits per node, as shown in the present teleportation experiment, makes NV centers a leading candidate for realizing a quantum network (6, 31). Our teleportation scheme is both unconditional and scalable to large distances, as it can mitigate photon loss by heralding and purification of the distributed entangled state (4). Our current capabilities could be supplemented with quantum memories that are robust against optical excitation of the elec-

trons, enabling remote entanglement purification (4, 32) and the connection of multiple nodes into the network. A promising route is the use of weakly coupled nuclear spins (33–35) on which multi-qubit quantum control has very recently been demonstrated (36). For such nuclear spins, coherence times of >1 s under optical excitation have been reported (37), while the incorporation of NV centers into optical cavities may enable remote entanglement generation on millisecond time scales (38). Furthermore, the entanglement and readout fidelities reported here are sufficient for a violation of a Bell inequality with the detection loophole closed, making NV centers a promising system for realizing a loophole-free Bell test and device-independent quantum key distribution (39).

REFERENCES AND NOTES

1. D. D. Awschalom, L. C. Bassett, A. S. Dzurak, E. L. Hu, J. R. Petta, *Science* **339**, 1174–1179 (2013).
2. M. H. Devoret, R. J. Schoelkopf, *Science* **339**, 1169–1174 (2013).
3. C. Monroe, J. Kim, *Science* **339**, 1164–1169 (2013).
4. H. J. Briegel, W. Dür, J. I. Cirac, P. Zoller, *Phys. Rev. Lett.* **81**, 5932–5935 (1998).
5. S. Barz et al., *Science* **335**, 303–308 (2012).
6. H. J. Kimble, *Nature* **453**, 1023–1030 (2008).
7. W. K. Wootters, W. H. Zurek, *Nature* **299**, 802–803 (1982).
8. C. H. Bennett et al., *Phys. Rev. Lett.* **70**, 1895–1899 (1993).
9. D. Bouwmeester et al., *Nature* **390**, 575–579 (1997).
10. A. Furusawa et al., *Science* **282**, 706–709 (1998).
11. S. Takeda, T. Mizuta, M. Fuwa, P. van Loock, A. Furusawa, *Nature* **500**, 315–318 (2013).
12. S. Olmschenk et al., *Science* **323**, 486–489 (2009).
13. C. Nölleke et al., *Phys. Rev. Lett.* **110**, 140403 (2013).
14. H. Krauter et al., *Nat. Phys.* **9**, 400–404 (2013).
15. M. Riebe et al., *Nature* **429**, 734–737 (2004).
16. M. D. Barrett et al., *Nature* **429**, 737–739 (2004).
17. L. Steffen et al., *Nature* **500**, 319–322 (2013).
18. L. Robledo et al., *Nature* **477**, 574–578 (2011).
19. G. de Lange, Z. H. Wang, D. Ristè, V. V. Dobrovitski, R. Hanson, *Science* **330**, 60–63 (2010).

20. S. D. Barrett, P. Kok, *Phys. Rev. A* **71**, 060310 (2005).
21. H. Bernien et al., *Nature* **497**, 86–90 (2013).
22. P. Siyushev et al., *Phys. Rev. Lett.* **110**, 167402 (2013).
23. Materials and methods are available at Science Online.
24. P. Neumann et al., *Science* **329**, 542–544 (2010).
25. L. Jiang et al., *Phys. Rev. Lett.* **100**, 073001 (2008).
26. M. S. Blok et al., *Nat. Phys.* **10**, 189–193 (2014).
27. T. van der Sar et al., *Nature* **484**, 82–86 (2012).
28. C. A. Ryan, J. S. Hodges, D. G. Cory, *Phys. Rev. Lett.* **105**, 200402 (2010).
29. B. Naydenov et al., *Phys. Rev. B* **83**, 081201 (2011).
30. S. Massar, S. Popescu, *Phys. Rev. Lett.* **74**, 1259–1263 (1995).
31. N. H. Nickerson, Y. Li, S. C. Benjamin, *Nat. Commun.* **4**, 1756 (2013).
32. L. Childress, J. M. Taylor, A. S. Sørensen, M. D. Lukin, *Phys. Rev. Lett.* **96**, 070504 (2006).
33. T. H. Taminiau et al., *Phys. Rev. Lett.* **109**, 137602 (2012).
34. S. Kolkowitz, Q. P. Unterreithmeier, S. D. Bennett, M. D. Lukin, *Phys. Rev. Lett.* **109**, 137601 (2012).
35. N. Zhao et al., *Nat. Nanotechnol.* **7**, 657–662 (2012).
36. T. H. Taminiau, J. Cramer, T. van der Sar, V. V. Dobrovitski, R. Hanson, *Nat. Nanotechnol.* **9**, 171–176 (2014).
37. P. C. Maurer et al., *Science* **336**, 1283–1286 (2012).
38. M. Lončar, A. Faraon, *MRS Bull.* **38**, 144–148 (2013).
39. N. Brunner, D. Cavalcanti, S. Pironio, V. Scarani, S. Wehner, *Rev. Mod. Phys.* **86**, 419–478 (2014).

ACKNOWLEDGMENTS

We thank L. Childress, L. DiCarlo, M. Hatridge, J. J. L. Morton, A. Reiserer, L. M. K. Vandersypen, and P. Walther for valuable discussions. We acknowledge support from the Dutch Organization for Fundamental Research on Matter (FOM), the Defense Advanced Research Projects Agency QuASAR program, the European Union DIAMANT and S3NANO programs, a Marie Curie Intra-European Fellowship, and the European Research Council through a Starting Grant.

SUPPLEMENTARY MATERIALS

www.sciencemag.org/content/345/6196/532/suppl/DC1
Materials and Methods
Figs. S1 to S6
Table S1
References (40–44)

18 March 2014; accepted 19 May 2014
Published online 29 May 2014;
10.1126/science.1253512

CHRONIC PAIN

Decreased motivation during chronic pain requires long-term depression in the nucleus accumbens

Neil Schwartz,¹ Paul Temkin,¹ Sandra Jurado,^{1,2} Byung Kook Lim,^{1,3} Boris D. Heifets,¹ Jai S. Polepalli,¹ Robert C. Malenka^{1*}

Several symptoms associated with chronic pain, including fatigue and depression, are characterized by reduced motivation to initiate or complete goal-directed tasks. However, it is unknown whether maladaptive modifications in neural circuits that regulate motivation occur during chronic pain. Here, we demonstrate that the decreased motivation elicited in mice by two different models of chronic pain requires a galanin receptor 1–triggered depression of excitatory synaptic transmission in indirect pathway nucleus accumbens medium spiny neurons. These results demonstrate a previously unknown pathological adaption in a key node of motivational neural circuitry that is required for one of the major sequela of chronic pain states and syndromes.

Symptoms that profoundly affect the quality of life of patients with chronic pain include fatigue, reductions in pre-pain activities, and depression (1–4). A common feature of these symptoms is a decrease in the motivation to undertake and to successfully complete goal-

directed actions. Although in the setting of acute pain these features may be adaptive by limiting activity during the healing process and reducing the likelihood of future injury by motivating avoidance (5, 6), they are a major source of the morbidity accompanying chronic pain syndromes. Here, we

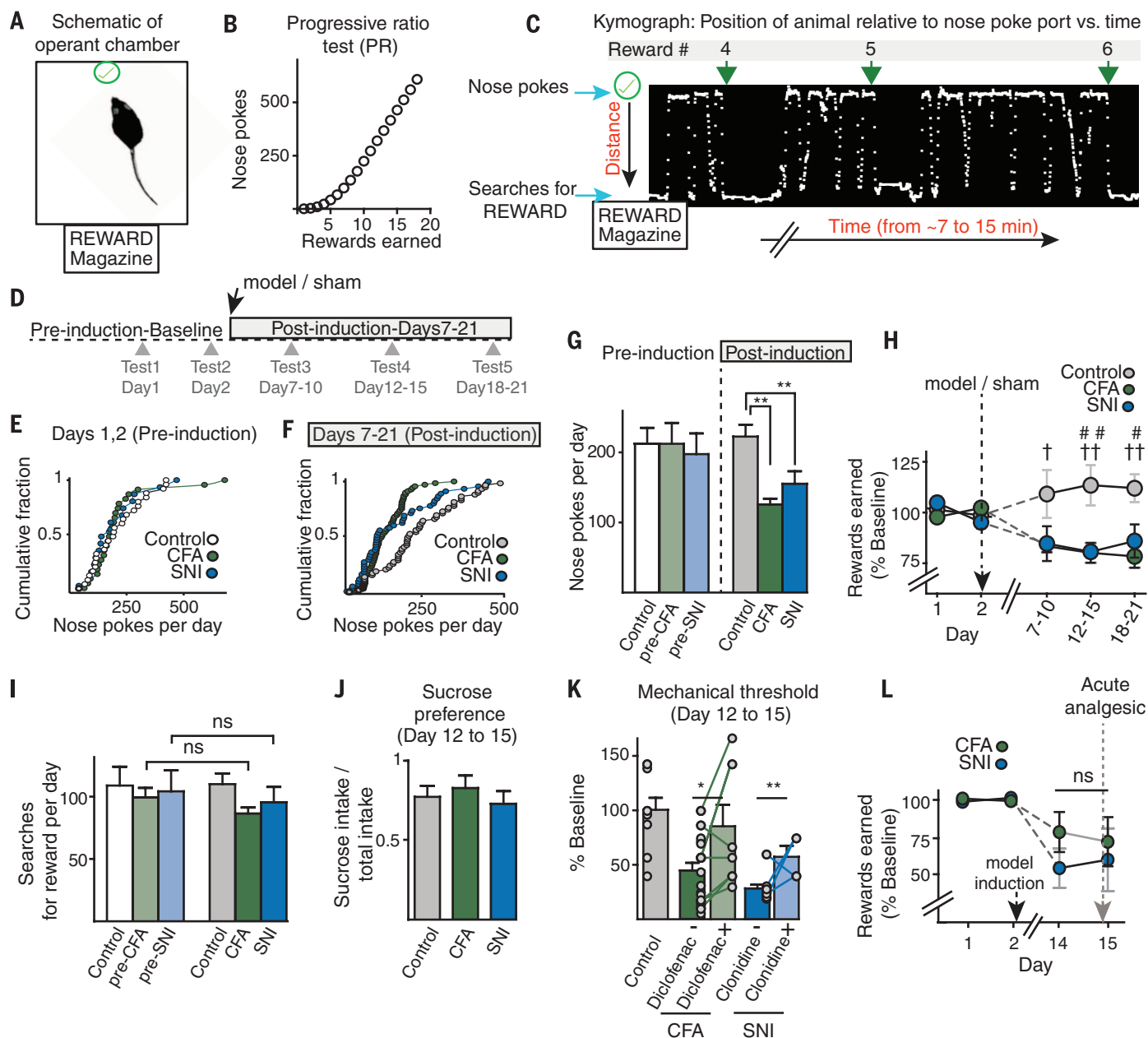


Fig. 1. Motivation is impaired in models of chronic pain. (A) Schematic of mouse in the operant chamber. (B) Sum of nose pokes required to earn rewards on PR schedule. (C) Kymograph illustrating distance from nose poke port (y axis) versus time (x axis). Green arrows indicate times at which rewards 4 to 6 were earned. (D) Time line of experiments. Results from 2 PR tests before induction of pain models were compared with results from 6 PR tests at three time points after induction. (E) Nose pokes per animal during 2 days of baseline testing. (F to H) Both CFA and SNI induction reduced number of nose pokes, resulting in a drop in the rewards earned at the respective time points (control, $n = 12$ mice, includes SNI sham surgery

$n = 4$, CFA sham injections $n = 5$, untreated $n = 3$; CFA $n = 10$ mice; SNI $n = 8$ mice). (G) $**P < 0.01$ versus control. (H) CFA $†P < 0.05$, $††P < 0.01$; SNI $##P < 0.05$, $###P < 0.01$; post hoc t tests. (I and J) During PR tests, there was no difference in searches for rewards before or after induction nor differences in the sucrose preference test (control $n = 6$ mice, CFA $n = 6$ mice, SNI $n = 5$ mice). (K) Both pain models reduce mechanical threshold, and this is ameliorated by analgesic administration (diclofenac, subcutaneous, $n = 8$ mice, $*P < 0.05$; clonidine, intrathecal, $n = 5$ mice, $**P < 0.01$; Student's t tests). (L) Neither acute analgesic affects the reduction in rewards earned after model induction. For all figures, error bars are SEM.

¹Nancy Pritzker Laboratory, Department of Psychiatry and Behavioral Sciences, Stanford University School of Medicine, 265 Campus Drive, Stanford, CA 94305, USA. ²Department of Pharmacology, School of Medicine, University of Maryland, 655 West Baltimore Street, Baltimore, MD 21201, USA. ³Neurobiology Section, Division of Biological Sciences, University of California, San Diego, La Jolla, CA 92093, USA.

*Corresponding author. E-mail: malenka@stanford.edu

hypothesize that like the maladaptive neural plasticity that contributes to somatosensory symptoms of chronic pain (7, 8), concurrent maladaptive plasticity occurs in neural circuits that regulate motivation. Therefore, we focused on the nucleus accumbens core (NAc) because it is a key node of the neural circuits mediating motivated behaviors (9–11), and activity within the human NAc

correlates with both the subjective experience of pain as well as the transition to chronic pain (12, 13).

Chronic pain reduces motivation in two mouse models

We used two mouse models of chronic pain (14, 15); chronic inflammatory pain induced by

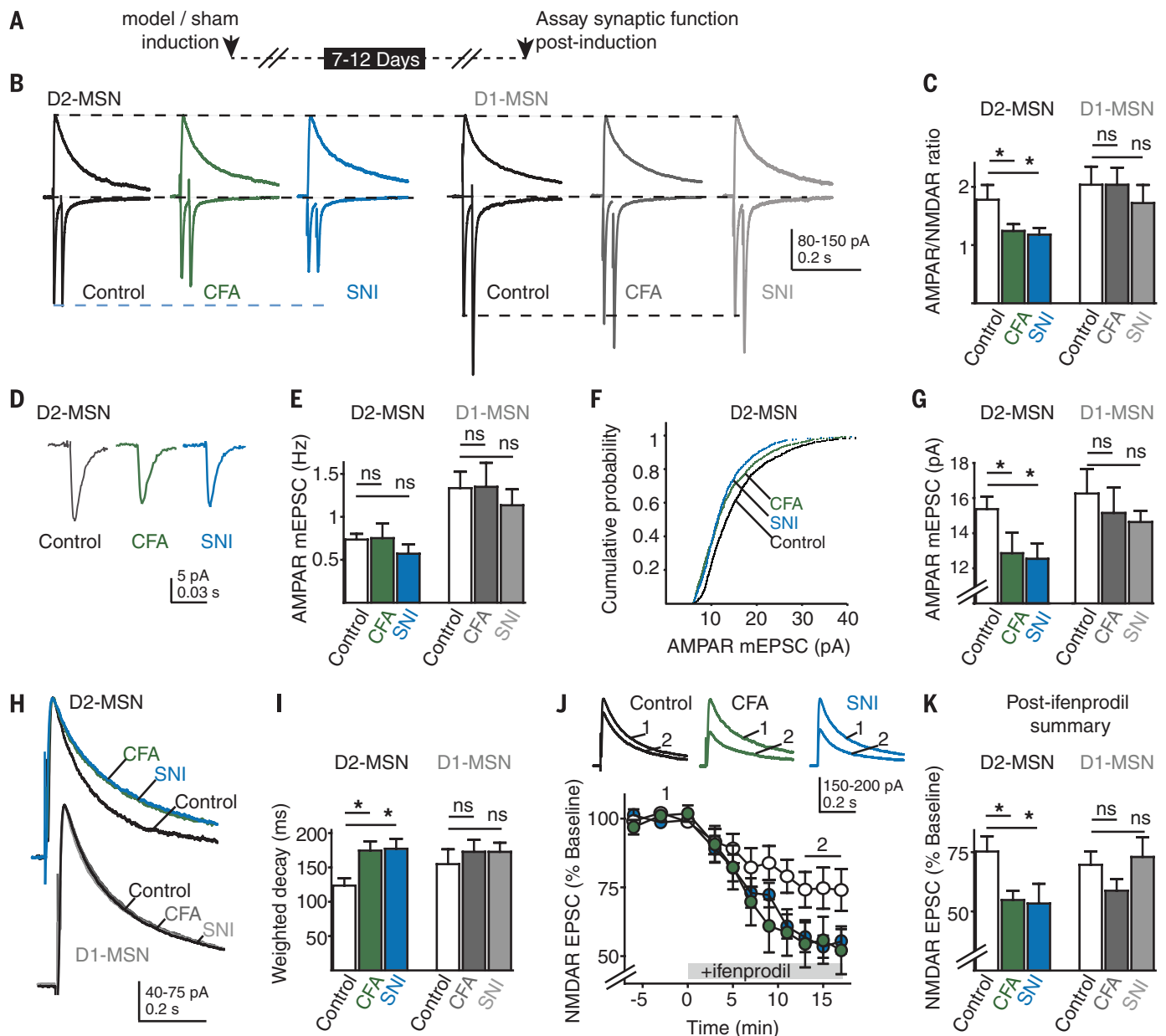


Fig. 2. Excitatory synapses are modified 7 to 12 days after induction of chronic pain. (A) Time course of experiments in (B) to (K). (B) Sample EPSCs recorded at +40 mV (top traces) and two EPSCs evoked with a 50-ms interval recorded at -70 mV (bottom traces) from NAc D2-MSNs and D1-MSNs at 7 to 12 days after sham procedures or after model induction. EPSC amplitudes are normalized to peaks at +40 mV. (C) Summary showing AMPAR/NMDAR ratios in D2-MSNs and D1-MSNs in both pain models (D2, control $n = 15$ cells, CFA $n = 13$ cells, SNI $n = 12$ cells; * $P < 0.05$ post hoc t test; D1, control $n = 12$ cells, CFA $n = 7$ cells, SNI $n = 11$ cells). (D) Average traces of 100 mEPSCs from representative D2-MSNs. (E) mEPSC frequency was unaffected by CFA and SNI treatments. (F and G) Cumulative distribution of mEPSC

amplitudes (F) and averages (G) in D2-MSNs and D1-MSNs in both pain models (D2, control $n = 14$ cells, CFA $n = 10$ cells, SNI $n = 12$ cells, * $P < 0.05$ Student's t test; D1, control $n = 13$ cells, CFA $n = 14$ cells, SNI $n = 13$ cells). (H) Sample normalized average traces of pharmacologically isolated NMDAR EPSCs. (I) Summary data of NMDAR EPSC decay kinetics from D2-MSNs and D1-MSNs in both pain models (D2, control $n = 12$ cells, CFA $n = 9$ cells, SNI $n = 6$ cells, * $P < 0.05$ post hoc t tests; D1, control $n = 9$ cells, CFA $n = 7$ cells, SNI $n = 12$ cells). (J and K) In both models, ifenprodil (3 μ M) caused a larger depression of NMDAR EPSCs in D2-MSNs versus D1-MSNs (D2, control $n = 8$ cells, CFA $n = 8$ cells, SNI $n = 6$ cells; D1, control $n = 9$ cells, CFA $n = 7$ cells, SNI $n = 5$ cells; * $P < 0.05$ post hoc t tests).

means of injection of complete Freund's adjuvant (CFA) into the hind paw and neuropathic pain induced by means of selective injury of the sciatic nerve (SNI). To measure motivation, we used a progressive ratio (PR) operant test in which it becomes progressively more difficult to earn each subsequent reward (16, 17). The point at which the

subject gives up provides a measure of motivation to work for reward (Fig. 1, A to C). Before inducing the models, all animals made a similar number of nose pokes and earned a comparable number of rewards (over the course of the 2-day baseline period) (Fig. 1, D and E, and fig. S1A). In contrast, 7 to 21 days after induction of chronic pain, animals

exhibited a ~40% drop in the number of nose pokes to earn rewards, resulting in a stable reduction in the rewards earned over the 3-week testing period (Fig. 1, F to H). There was no change in the number of searches for reward (Fig. 1I), implying that animals exhibited no change in their ability to cross the chamber to

search for the reward and no change in their perceived value of the reward.

To further test the animals' valuation of rewards, on day 22 after pain induction, animals were tested on a fixed ratio 1 (FR1) schedule of reward, during which each nose poke earns a reward. Under this schedule, all groups earned the maximum number of rewards (30) at the same rate and searched for rewards a comparable number of times (fig. S1B). Similarly, neither model affected sucrose preference (Fig. 1J) or food consumption (fig. S1C).

Last, although the mechanical threshold of the animal did not predict its level of impairment on the PR task (fig. S2), we asked whether acutely suppressing the somatosensory symptoms of the models would ameliorate the observed reduction in motivation. In two subsets of animals after CFA and after SNI induction, the analgesics diclofenac and clonidine, respectively, were administered before testing on day 15. Despite an increase in paw withdrawal thresholds in both pain models (Fig. 1K), neither acute analgesic ameliorated performance on the PR task (Fig. 1L).

Chronic pain elicits synaptic modifications in nucleus accumbens

To determine whether chronic pain elicits synaptic changes in NAc circuitry, we prepared brain slices from bacterial artificial chromosome (BAC) transgenic animals and made targeted whole-cell recordings from visually identified medium spiny neurons (MSNs) belonging to either the direct pathway, D1 dopamine receptor expressing MSNs (D1-MSNs), or the indirect pathway, D2

dopamine receptor expressing MSNs (D2-MSNs) (18). We first calculated the ratio of α -amino-3-hydroxy-5-methyl-4-isoxazolepropionic acid receptor (AMPA)-mediated excitatory postsynaptic currents (EPSCs) to *N*-methyl-D-aspartate receptor (NMDAR)-mediated EPSCs (AMPA/NMDAR ratio). Seven to 12 days after either CFA injection or SNI surgery, this ratio was significantly lower in NAc D2-MSNs but was unchanged in NAc D1-MSNs (Fig. 2, A to C). This decrease in the two models was at least in part due to a decrease in the number and/or function of AMPARs because the amplitude of miniature EPSCs (mEPSCs) was decreased in D2-MSNs but not in D1-MSNs (Fig. 2, D, F, and G). In contrast, assays of presynaptic function were not affected in either model (Fig. 2E and fig. S3).

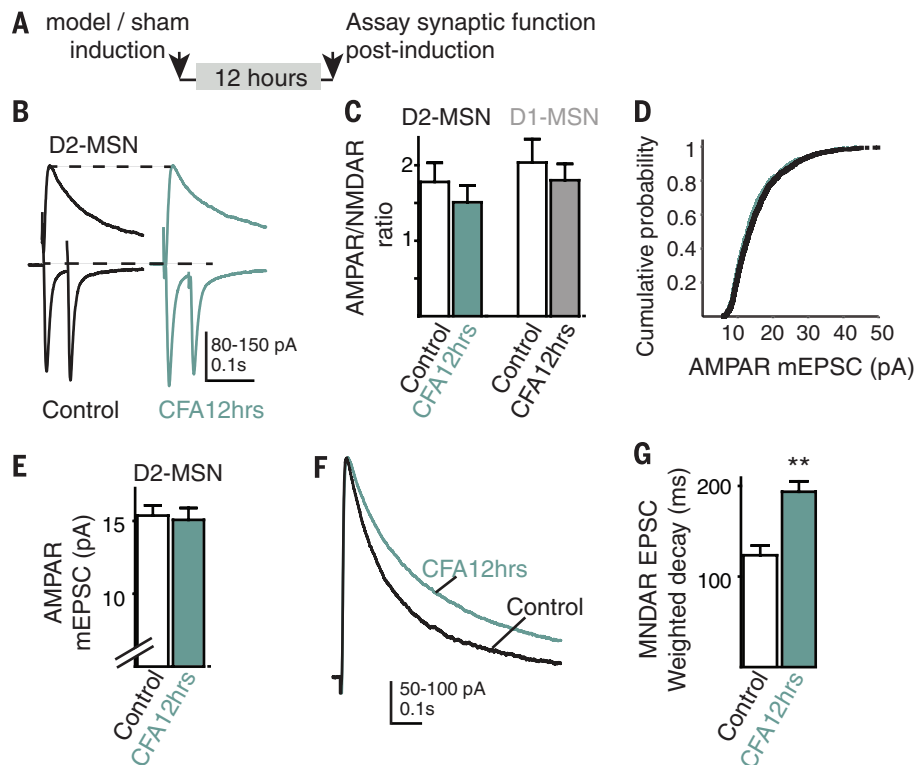
The fractional decrease for D2-MSN mEPSC amplitudes in both models was less than the fractional decrease in the AMPAR/NMDAR ratios, suggesting that chronic pain may have also affected NMDAR-mediated synaptic transmission. We therefore recorded pharmacologically isolated NMDAR EPSCs and found that their time constant of decay was prolonged in D2-MSNs, but not D1-MSNs, in NAc slices prepared 7 to 12 days after model induction (Fig. 2, H and I). Prolonged NMDAR EPSC decay kinetics are normally due to an increase in the proportion of synaptic NMDARs containing the GluN2B subunit (19). We confirmed this possibility; the GluN2B antagonist ifenprodil caused a larger depression of NMDAR EPSCs in D2-MSNs 7 to 12 days after induction as compared with that of controls (Fig. 2, J and K). This difference was not observed in D1-MSNs (Fig. 2K).

In the early stages of withdrawal from drugs of abuse, a change in the stoichiometry of synaptic NMDARs in MSNs can be observed, and this is followed at later time points by modulation of AMPAR-mediated transmission (20). To determine whether similar changes occur at the onset of the pain experience, we repeated the assays of synaptic function at 12 hours after injection of CFA (CFA12hrs). At this early time point, AMPAR-mediated synaptic transmission was unchanged compared with controls (Fig. 3, A to E), yet NMDAR EPSCs exhibited prolonged decay kinetics in D2-MSNs (Fig. 3, F and G).

Galanin is required for pain-induced synaptic modifications in NAc

In several brain regions, activation of G protein-coupled receptors (GPCRs) by different neuromodulators causes changes in synaptic NMDAR stoichiometry (19). We investigated the possible role of the neuropeptide galanin (Gal) in the pain-induced changes in NMDAR stoichiometry in NAc D2-MSNs for several reasons. In patients, polymorphisms affecting Gal signaling predict the development of comorbidities during chronic pain, increased reactivity in the NAc to rewards, and poor resilience to long-term stress (21–24). In rodents, intraventricular infusion of Gal reduces performance on a PR task (25), and in several pain models, Gal is up-regulated in brain regions that project to NAc (26–29). We observed Gal-positive neurons, which were retrogradely labeled by a rabies virus injected into the NAc (30), in several brain regions (Fig. 4A). Also consistent with previous studies (31, 32), in both D1-MSNs and D2-MSNs Gal (1 μ M) caused

Fig. 3. NMDAR EPSCs are slower in D2-MSNs 12 hours after induction of chronic pain. (A) Experimental protocol. (B) Sample EPSCs from D2-MSNs recorded 12 hours after saline (control) or CFA injection (CFA12hrs). Traces are normalized to peak at +40 mV. (C) Summary of AMPAR/NMDAR ratios in D2-MSNs and D1-MSNs at this time point (D2, control, $n = 15$ cells, CFA12hrs $n = 12$ cells; D1, control $n = 12$ cells, CFA12hrs $n = 9$ cells). (D and E) Cumulative distribution and average of mEPSC amplitudes from D2-MSNs at this time point (control $n = 14$ cells, CFA12hrs $n = 10$ cells). (F) Sample normalized average NMDAR EPSCs from D2-MSN neurons. (G) Summary of NMDAR EPSC weighted decay time constants 12 hours after CFA (control $n = 12$ cells; CFA12hrs $n = 16$ cells; $**P < 0.01$ Student's *t* test).



a transient, presynaptic decrease in excitatory transmission, which was unaffected by loading MSNs with guanosine 5'-O-(2'-thiodiphosphate) (GDP- β -S) to inhibit GPCR signaling in postsynaptic compartments (Fig. 4B and figs. S4 and S5) (31). In contrast to this transient change, the decay kinetics of NMDAR EPSCs in D2-MSNs but not D1-MSNs were prolonged after Gal application (Fig. 4C and fig. S5). This change in NMDAR EPSC decay kinetics was blocked by postsynaptic GDP- β -S (fig. S5) and was accompanied by an increase in the magnitude of the NMDAR EPSC depression caused by ifenprodil in D2-MSNs only (Fig. 4D).

To directly test whether Gal signaling within the NAc is required for the change in NMDAR EPSC kinetics in D2-MSNs, we used two complementary approaches. In one set of animals, we infused the galanin receptor 1,2 (GalR1,2) antagonist M40 (0.4 μ g μ L⁻¹) into the NAc

preceding and during the 12-hour period after CFA treatment. In another set of animals, before CFA treatment we expressed an effective short hairpin RNA (shRNA) to GalR1 in the NAc bilaterally because GalR1, but not GalR2, has been implicated in regulating motivation (Fig. 4E) (25). We chose CFA injections because the symptoms develop and plateau rapidly, producing a temporally more well-defined model of chronic pain (14, 33). Both manipulations prevented the increase in NMDAR EPSC decay kinetics in D2-MSNs normally caused by CFA treatments, whereas intra-NAc injection of vehicle alone did not (Fig. 4, F to H). Furthermore, knockdown of GalR1 prevented the increased sensitivity to ifenprodil caused by CFA injection (Fig. 4I).

The results thus far suggest that during the onset of chronic pain, Gal in the NAc signals through GalR1 to increase the synaptic fraction of GluN2B in D2-MSNs. Then over the ensuing

1 to 2 weeks, AMPAR-mediated synaptic transmission progressively decreases. In other brain regions, a similar change in NMDAR stoichiometry has been suggested to reduce the threshold for induction of long-term depression (LTD) of AMPAR-mediated transmission (34). Consistent with this hypothesis, preincubating NAc slices in Gal increased the magnitude of LTD elicited in D2-MSNs (fig. S6, A to C). NMDAR-dependent LTD in control slices was blocked by D-AP5 (fig. S6, D and E) but was unaffected by ifenprodil, whereas in Gal-treated slices, ifenprodil strongly inhibited LTD (fig. S7). Three findings suggest that similar events occur in vivo in the NAc in the pain models. First, in both models knockdown of GalR1 in vivo prevented the decrease in AMPAR/NMDAR ratios in NAc D2-MSNs (Fig. 5, A and B). Second, NMDAR-dependent LTD in D2-MSNs was reduced—presumably occluded—in slices prepared from animals 7 to 12 days after model

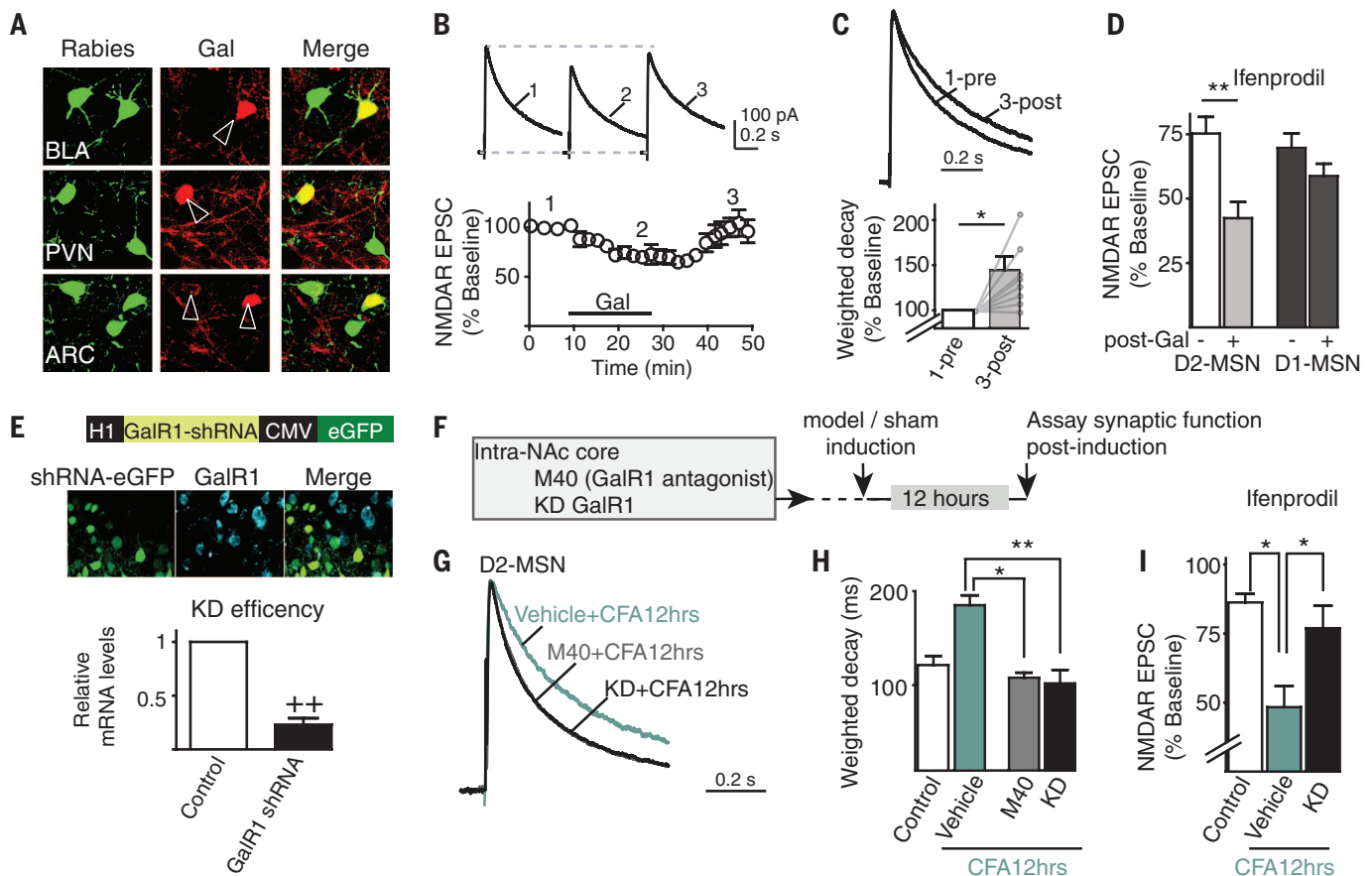


Fig. 4. Increase in NMDAR EPSC decay 12 hours after induction of chronic pain requires GalR1. (A) Images of neurons retrogradely labeled by rabies virus expressing eGFP (green) injected into NAc overlaid with Gal-antibody labeling (red) from basolateral amygdala (BLA), paraventricular nucleus of thalamus (PVN), and arcuate nucleus of hypothalamus (ARC). (B) Sample NMDAR EPSCs from D2-MSN taken at time points indicated on summary graph showing transient effects of Gal (1 μ M). (C) Summary of change in NMDAR EPSC decay kinetics after wash-out of Gal ($n = 8$ cells; $*P < 0.05$ repeated measure t test). (D) Ifenprodil causes larger depression of NMDAR EPSCs in D2-MSNs versus D1-MSNs from slices preincubated in Gal (D2, nontreated from Fig. 2K, post-Gal+ $n = 6$ cells; D1, nontreated from Fig. 2K, post-Gal+ $n = 6$ cells; $**P < 0.01$ Student's t test). (E)

Schematic of adeno-associated virus vector expressing GalR1 shRNA and eGFP, with images showing eGFP expression and GalR1 staining 1 month after infection of NAc. Graph shows relative mRNA levels from sister hippocampal cultures infected with eGFP and GalR1 shRNA, respectively ($n = 3$ experiments; $++P = 0.006$ Student's t test). (F) Time line of experiments in (G) to (I). (G) Sample normalized NMDAR EPSCs from D2-MSNs. (H) Summary graph of NMDAR EPSC decay kinetics 12 hours after CFA. KD, knockdown. (D2, control taken from Fig. 3, vehicle+CFA12hrs $n = 9$ cells, M40 +CFA12hrs $n = 12$ cells, KD+CFA12hrs $n = 8$ cells; $**P < 0.01$, $*P < 0.05$ post hoc t tests). (I) Effects of ifenprodil on NMDAR EPSCs 12 hours after CFA (control $n = 8$ cells, Vehicle+CFA12hrs $n = 5$ cells, KD+CFA12hrs $n = 5$ cells; $*P < 0.05$ post hoc t test).

induction (Fig. 5, C to E). Third, the reduction in LTD that occurs in the chronic-pain models was reversed in D2-MSNs in which knockdown of GalR1 occurred (Fig. 5, D and E).

NAc synaptic modifications required for decreased motivation during chronic pain

To determine whether GalR1-dependent synaptic changes in NAc are necessary for the decreased motivation accompanying the chronic pain models, we performed behavioral assays in animals that had been injected bilaterally into the NAc with viruses expressing enhanced green fluorescent protein (eGFP) alone, the GalR1 shRNA, or the GalR1 shRNA along with a GalR1-eGFP replacement construct (Rep.GalR1 KD) (Fig. 5, F and G). Behavior during baseline PR testing was similar between groups (Fig. 5H), and after model induction, a new set of control animals (uninjected or expressing eGFP alone) showed comparable decreases in motivation to nose poke for rewards (Fig. 5, I and J). Therefore, these groups were combined. Knockdown of GalR1 bilaterally in the NAc ameliorated the decrease in motivation normally caused by both pain models (Fig. 5, I and J), whereas expression of the Rep. GalR1 knockdown in CFA-treated animals returned their behavior to that resembling control

animals: They exhibited a decrease in nose pokes after model induction (Fig. 5I). To limit the expression of the replacement GalR1 construct to indirect pathway NAc MSNs, we injected a CRE-dependent Rep.GalR1 KD construct into the NAc of Adenosine A2a CRE mice, in which CRE expression is limited to D2-MSNs (35). These animals exhibited a decrease in nose pokes after SNI comparable with the decrease observed in controls after SNI (fig S8). Somatosensory symptoms and other measures of operant behavior were not affected by the knockdown of GalR1 in either model (fig. S9).

To determine whether the depression of AMPAR-mediated transmission and reduction/occlusion of LTD were required for the pain-induced behavioral changes, we took advantage of the finding that NMDAR-dependent LTD depends on the appropriate synaptic positioning of the critical phosphatase calcineurin (PP2B) by the scaffolding protein A-kinase anchoring protein 79/150 (AKAP) (36). Thus, we knocked down AKAP in the NAc and replaced it with a mutant AKAP that does not bind PP2B (AKAPΔPP2B), a manipulation that blocks LTD in the hippocampus (36). This manipulation inhibited LTD in NAc MSNs, whereas replacement of AKAP with a shRNA-resistant wild-type AKAP (AKAPWT)

did not (Fig. 6, A to C). Although the basal AMPAR/NMDAR ratio in D2-MSNs was not affected by AKAPΔPP2B, the decrease in this ratio elicited by the CFA model was inhibited (Fig. 6D).

Next, we repeated the behavioral experiments in animals expressing the AKAP replacement constructs in the NAc bilaterally (Fig. 6E). These manipulations did not affect the behavioral responses during baseline PR testing (Fig. 6F and fig. S10). However, whereas animals expressing control constructs (AKAPWT and eGFP) exhibited the expected decrease in nose pokes after model induction, animals expressing AKAPΔPP2B showed no deficits in performance (Fig. 6, G and H). Thus, in two different pain models, two different molecular manipulations (GalR1 knockdown and AKAPΔPP2B), which prevented chronic pain-induced modifications of excitatory synapses on NAc D2-MSNs via completely independent mechanisms, prevented pain-induced motivational impairments (Fig. 6I) while having no effect on mechanical thresholds or other measures of operant goal-directed behaviors (figs. S9 and S10).

Discussion

The NAc is a key node of the neural circuitry that regulates motivation (10). Manipulations that disrupt its activity appear to impair performance on

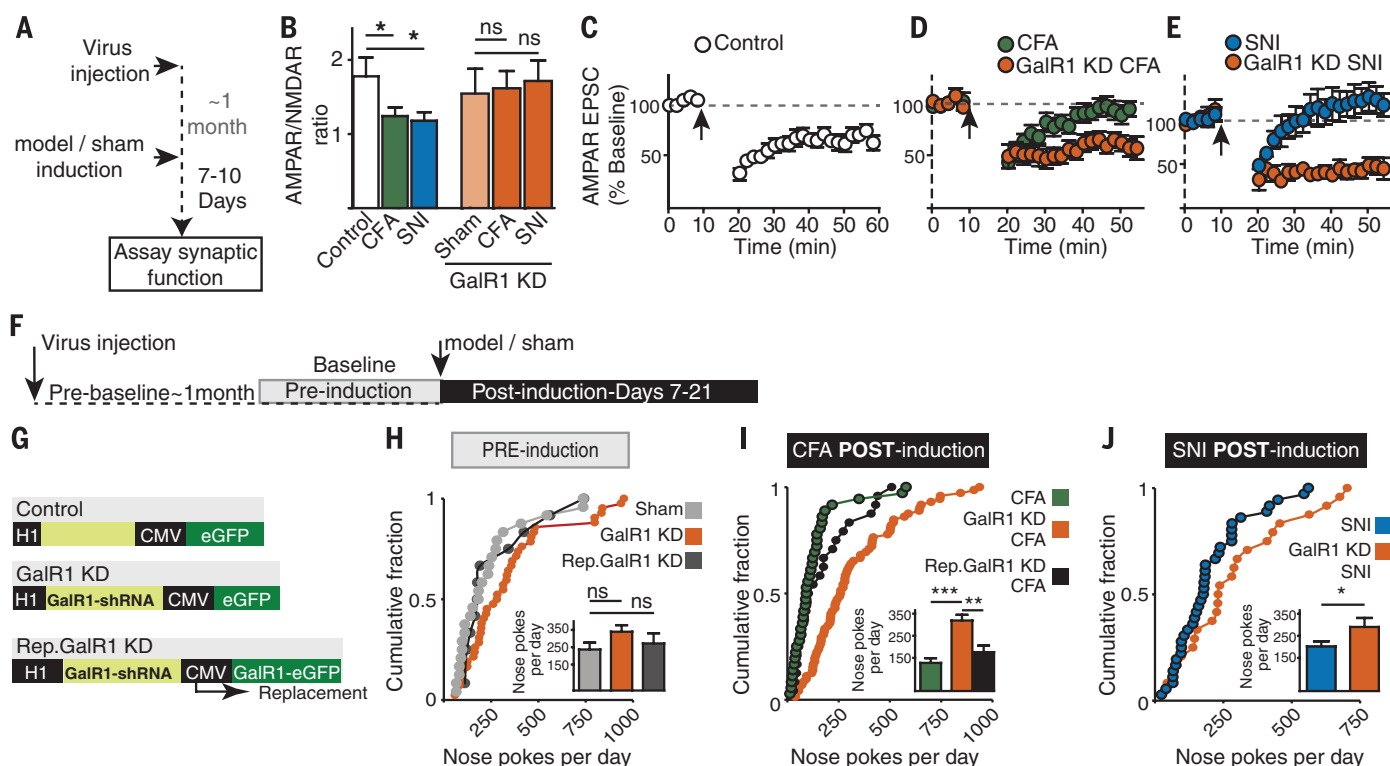


Fig. 5. GalR1 in NAc is required for pain-induced synaptic depression in D2-MSNs and reduction in motivation. (A) Time line of acute slice experiments in (B) to (E). (B) Decrease in AMPAR/NMDAR ratios in D2-MSNs in both pain models is prevented by GalR1 KD [control, CFA and SNI (left group) taken from Fig. 2; GalR1 KD, sham $n = 5$ cells, CFA $n = 11$ cells, SNI $n = 8$ cells]. (C to E) Summary graphs of LTD in D2-MSNs in both pain models and effects of GalR1 KD (control, $n = 11$ cells, CFA $n = 10$ cells, GalR1 KD+CFA $n = 7$ cells, SNI $n = 6$ cells, GalR1 KD+SNI $n = 6$ cells). (F) Timeline of behavior experiments in (H) to (J). (G) Schematics of virus constructs. (H) Cumulative distribution of

nose pokes per session and average nose pokes per day during before-induction baseline period (PRE). (sham $n = 12$ mice includes eGFP $n = 5$ mice, naive $n = 7$ mice; GalR1 KD $n = 18$ mice, Rep. GalR1 KD $n = 6$ mice). (I and J) Effects of GalR1 KD in NAc on nose pokes after model induction and rescue by coexpression of shRNA-resistant GalR1 (Rep.GalR1 KD) in CFA model. (I) CFA $n = 6$ mice includes eGFP $n = 3$ mice, naive $n = 3$ mice; GalR1 KD+CFA $n = 12$ mice, Rep. GalR1 KD+CFA $n = 6$ mice, $^{**}P < 0.01$, $^{***}P < 0.001$ Tukey's post hoc t test. (J) SNI $n = 6$ mice includes eGFP $n = 2$ mice, naive $n = 4$ mice; GalR1 KD+SNI $n = 6$ mice, $^{*}P < 0.05$ Student's t test.

more difficult operant tasks but have little effect on the performance of easy operant tasks, perhaps because impairments of NAc function bias behavioral choices to those that require less effort (9, 37–39). Here, we demonstrate that two different chronic pain models cause a selective impairment in performance on a difficult PR task but have no detectable effects on easier tasks or the value of rewards. This chronic pain-induced decrease in motivation requires a decreased excitatory drive onto indirect pathway

NAc MSNs downstream of activation of the neuropeptide receptor GalR1 via a cascade of synaptic modifications (Fig. 6J).

Simple models proposing a dichotomous role for striatal indirect and direct pathways have been useful in generating hypotheses with which to describe the circuit adaptations underlying behaviors associated with models of addiction and depression (30, 40). However, they are inadequate to account for the diverse actions of neuropeptides on NAc synaptic and circuit func-

tion (30, 41–44) as well as the neuronal activity observed during operant behaviors (45, 46). Nonetheless, the present findings—along with the observations that reductions in effortful behavior are caused by blocking D2 receptors in NAc and that these effects can be reversed by A2a receptor antagonists (38, 39)—support a key role of NAc D2-MSNs in regulating performance during more difficult tasks. Because the NAc integrates inputs from multiple structures, future studies will need to address the critical question of whether the

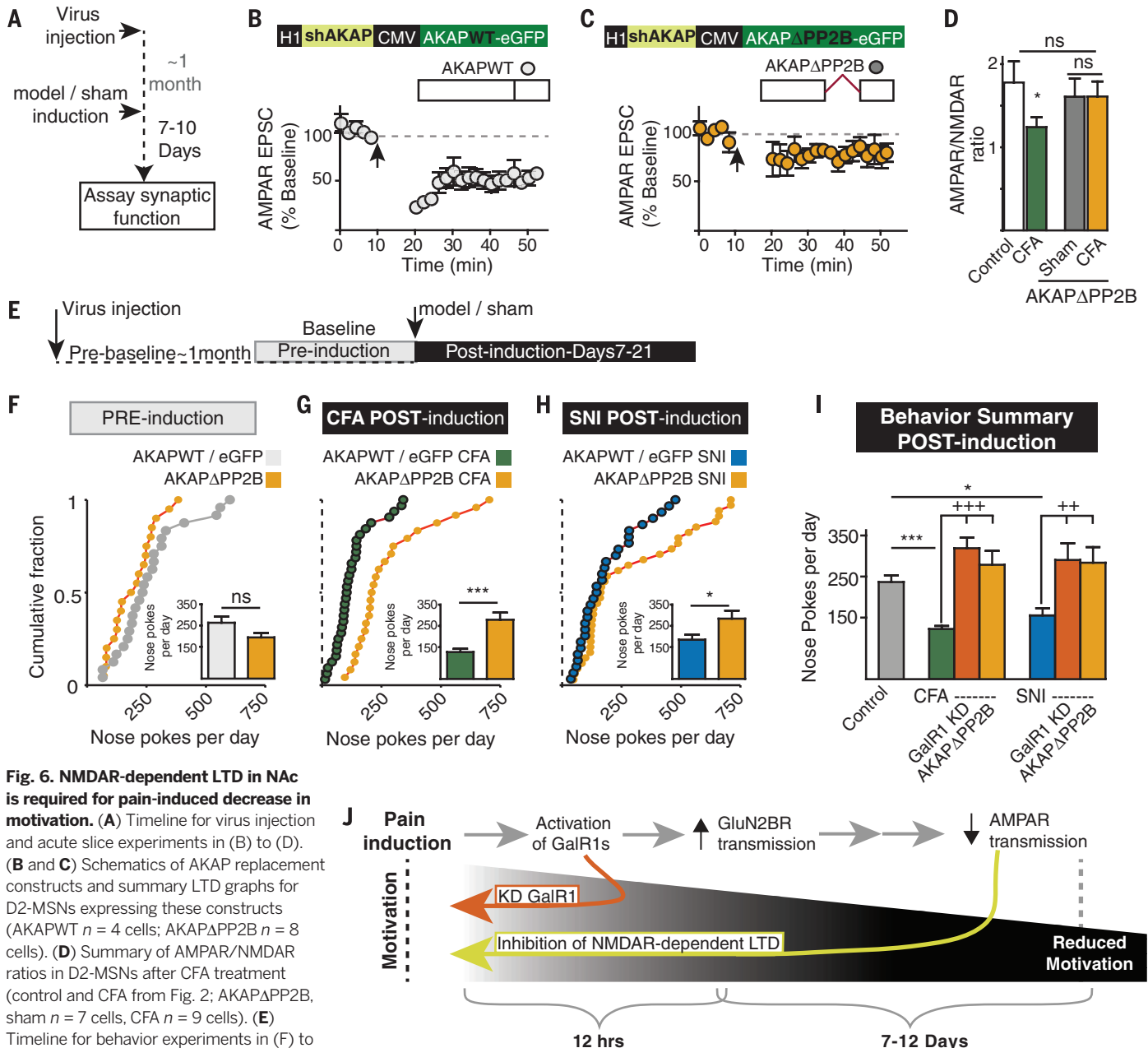


Fig. 6. NMDAR-dependent LTD in NAc is required for pain-induced decrease in motivation.

(A) Timeline for virus injection and acute slice experiments in (B) to (D). (B and C) Schematics of AKAP replacement constructs and summary LTD graphs for D2-MSNs expressing these constructs (AKAPWT $n = 4$ cells; AKAPΔPP2B $n = 8$ cells). (D) Summary of AMPAR/NMDAR ratios in D2-MSNs after CFA treatment (control and CFA from Fig. 2; AKAPΔPP2B, sham $n = 7$ cells, CFA $n = 9$ cells). (E) Timeline for behavior experiments in (F) to (I). (F to H) Cumulative distribution of nose pokes per session and average nose pokes per day during before-induction baseline (PRE) and after model induction (POST). (F) AKAPWT/eGFP $n = 13$ mice includes eGFP $n = 5$ mice, AKAPWT $n = 8$ mice; AKAPΔPP2B $n = 10$ mice. (G) AKAPWT/eGFP CFA $n = 7$ mice includes eGFP $n = 3$ mice, AKAPWT, $n = 4$ mice; AKAPΔPP2B+CFA $n = 4$. (H) AKAPWT/eGFP SNI $n = 6$ mice includes eGFP $n = 2$ mice, AKAPWT $n = 4$ mice; AKAPΔPP2B+SNI $n = 6$

mice; * $P < 0.05$, *** $P < 0.001$ Student's t test. (I) Summary of effects of GalR1 KD and AKAPΔPP2B expression on nose pokes per day after model induction (data pooled from Figs. 1, 5, and 6) (* $P < 0.05$, *** $P < 0.001$ post hoc t test versus control; ++ $P < 0.01$, +++ $P < 0.001$ Tukey's post hoc t test versus respective pain model). (J) Schematic summarizing temporal order of synaptic and behavioral changes after pain induction.

chronic pain-induced synaptic changes are global, affecting all excitatory inputs onto MSNs, or rather are input-specific.

Previous studies on mouse models of chronic pain report no change in home cage behaviors or measures of affective behaviors during the first month of the pathology (14, 15). Within a similar time frame, by focusing on a more subtle aspect of goal-directed operant behavior—the motivation to work for natural reward—we found that motivation was impaired. Our results suggest that pain-induced synaptic adaptations within the NAc contribute to a subjective impairment in the ability to initiate or sustain physical or mental tasks (47, 48), or to the symptom of central fatigue commonly reported by chronic pain patients (1, 2). These results also suggest specific synaptic targets that may be susceptible to therapeutic interventions.

REFERENCE AND NOTES

1. B. Nicholson, S. Verma, *Pain Med.* **5**, S9–S27 (2004).
2. D. C. Turk, J. Audette, R. M. Levy, S. C. Mackey, S. Stanos, *Mayo Clin. Proc.* **85**, S42–S50 (2010).
3. J. Dershi, P. B. Polatin, R. J. Gatchel, *Psychosom. Med.* **64**, 773–786 (2002).
4. T. Jonsson et al., *Acta Anaesthesiol. Scand.* **55**, 69–74 (2011).
5. J. P. Johansen, H. L. Fields, B. H. Manning, *Proc. Natl. Acad. Sci. U.S.A.* **98**, 8077–8082 (2001).
6. D. Borsook et al., *Eur. J. Pain* **11**, 7–20 (2007).
7. C. A. von Hehn, R. Baron, C. J. Woolf, *Neuron* **73**, 638–652 (2012).
8. A. I. Basbaum, D. M. Bautista, G. Scherrer, D. Julius, *Cell* **139**, 267–284 (2009).
9. J. D. Salamone, M. Correa, *Neuron* **76**, 470–485 (2012).
10. G. J. Mogenson, D. L. Jones, C. Y. Yim, *Prog. Neurobiol.* **14**, 69–97 (1980).
11. B. W. Balleine, J. P. O'Doherty, *Neuropsychopharmacology* **35**, 48–69 (2010).
12. D. J. Scott, M. M. Heitzeg, R. A. Koeppe, C. S. Stohler, J.-K. Zubieta, *J. Neurosci.* **26**, 10789–10795 (2006).
13. M. N. Baliki et al., *Nat. Neurosci.* **15**, 1117–1119 (2012).
14. R. Urban, G. Scherrer, E. H. Goulding, L. H. Tecott, A. I. Basbaum, *Pain* **152**, 990–1000 (2011).
15. I. Yalcin et al., *Biol. Psychiatry* **70**, 946–953 (2011).
16. H. S. Roane, *J. Appl. Behav. Anal.* **41**, 155–161 (2008).
17. C. P. O'Brien, E. L. Gardner, *Pharmacol. Ther.* **108**, 18–58 (2005).
18. J. A. Shuen, M. Chen, B. Gloss, N. Calakos, *J. Neurosci.* **28**, 2681–2685 (2008).
19. A. Sanz-Clemente, R. A. Nicoll, K. W. Roche, *Neuroscientist* **19**, 62–75 (2013).
20. B. R. Lee, Y. Dong, *Neuropharmacology* **61**, 1060–1069 (2011).
21. M. B. Max et al., *Mol. Pain* **2**, 14 (2006).
22. P. G. Unschuld et al., *J. Affect. Disord.* **105**, 177–184 (2008).
23. N. R. Wray et al., *Mol. Psychiatry* **17**, 36–48 (2012).
24. Y. S. Nikolova, E. K. Singhi, E. M. Drabant, A. R. Hariri, *Genes Brain Behav.* **12**, 516–524 (2013).
25. M. E. Anderson, J. Runesson, I. Saar, U. Langel, J. K. Robinson, *Behav. Brain Res.* **239**, 90–93 (2013).
26. V. Sergeev, C. Broberger, T. Hökfelt, *Brain Res. Mol. Brain Res.* **90**, 93–100 (2001).
27. H. Imbe et al., *Neurosci. Lett.* **368**, 102–106 (2004).
28. H. Nishii, M. Nomura, H. Aono, N. Fujimoto, T. Matsumoto, *Regul. Pept.* **141**, 105–112 (2007).
29. X.-L. Gu, Y.-G. Sun, L.-C. Yu, *Behav. Brain Res.* **179**, 331–335 (2007).
30. B. K. Lim, K. W. Huang, B. A. Grueter, P. E. Rothwell, R. C. Malenka, *Nature* **487**, 183–189 (2012).
31. Y. Dong, J. P. Tyszkiewicz, T. M. Fong, *J. Neurophysiol.* **95**, 3228–3234 (2006).
32. E. B. Einstein, Y. Asaka, M. F. Yeckel, M. J. Higley, M. R. Picciotto, *Eur. J. Neurosci.* **37**, 1541–1549 (2013).
33. E. J. Cobos et al., *Pain* **153**, 876–884 (2012).
34. K. Yashiro, B. D. Philpot, *Neuropharmacology* **55**, 1081–1094 (2008).
35. P. F. Dierux et al., *Nat. Neurosci.* **12**, 393–395 (2009).
36. S. Jurado, V. Biou, R. C. Malenka, *Nat. Neurosci.* **13**, 1053–1055 (2010).
37. S. M. Nicola, *J. Neurosci.* **30**, 16585–16600 (2010).
38. A. M. Farrar et al., *Neuroscience* **166**, 1056–1067 (2010).
39. J. L. Santerre et al., *Pharmacol. Biochem. Behav.* **102**, 477–487 (2012).
40. M. K. Lobo, E. J. Nestler, *Front. Neuroanat.* **5**, 41 (2011).
41. J. C. Lemos et al., *Nature* **490**, 402–406 (2012).
42. B. B. Land et al., *J. Neurosci.* **28**, 407–414 (2008).
43. G. Dölen, A. Darvishzadeh, K. W. Huang, R. C. Malenka, *Nature* **501**, 179–184 (2013).
44. M. Marinelli, P. V. Piazza, *Eur. J. Neurosci.* **16**, 387–394 (2002).
45. G. Cui et al., *Nature* **494**, 238–242 (2013).
46. F. Kasanetz et al., *Science* **328**, 1709–1712 (2010).
47. A. Chaudhuri, P. O. Behan, *Lancet* **363**, 978–988 (2004).
48. K. B. Norheim, G. Jonsson, R. Omdal, *Rheumatology (Oxford)* **50**, 1009–1018 (2011).

ACKNOWLEDGMENTS

We thank members of the Malenka lab for helpful feedback and comments during the study. We thank S. Fang and A. Darvishzadeh for help with stereotaxic injections and P. Rothwell for setting up the operant behavior chambers and software. This work was supported by a Banting postdoctoral fellowship (N.S.) and the NIH (R.C.M.). All primary data (behavioral, electrophysiological, and immunohistochemical) are archived in the Department of Psychiatry and Behavioral Sciences, Stanford University School of Medicine.

SUPPLEMENTARY MATERIALS

www.sciencemag.org/content/345/6196/535/suppl/DC1
Materials and Methods

Figs. S1 to S10
References (49–54)

27 March 2014; accepted 12 June 2014
10.1126/science.1253994

REPORTS

PHOTOVOLTAICS

Interface engineering of highly efficient perovskite solar cells

Huanping Zhou,^{1,2*} Qi Chen,^{1,2*} Gang Li,¹ Song Luo,^{1,2} Tze-bing Song,^{1,2} Hsin-Sheng Duan,^{1,2} Ziruo Hong,¹ Jingbi You,¹ Yongsheng Liu,^{1,2} Yang Yang^{1,2†}

Advancing perovskite solar cell technologies toward their theoretical power conversion efficiency (PCE) requires delicate control over the carrier dynamics throughout the entire device. By controlling the formation of the perovskite layer and careful choices of other materials, we suppressed carrier recombination in the absorber, facilitated carrier injection into the carrier transport layers, and maintained good carrier extraction at the electrodes. When measured via reverse bias scan, cell PCE is typically boosted to 16.6% on average, with the highest efficiency of ~19.3% in a planar geometry without antireflective coating. The fabrication of our perovskite solar cells was conducted in air and from solution at low temperatures, which should simplify manufacturing of large-area perovskite devices that are inexpensive and perform at high levels.

Organic-inorganic hybrid materials, particularly the perovskite family, have shown great promise for use in field-effect transistors, light-emitting diodes, sensors, and photodetectors for more than a decade (1). Recently, the power conversion efficiency (PCE)

of lead halide perovskite (CH₃NH₃PbX₃, X = Cl, Br, I)-based thin film photovoltaic devices has skyrocketed from 3.8% to more than 17% in just 4 years (2–6). In a typical perovskite solar cell, a several-hundred-nanometer-thick absorber layer, either with or without mesoporous scaffold, is

sandwiched between the electron and hole transport layers (ETLs and HTLs, respectively). Upon the absorption of incident photons, carriers are created in the absorber that travel through a transport pathway including the ETL or HTL, the electrodes, and each interface in between. To increase the PCE, it is essential to precisely manipulate carriers along the entire pathway from the absorber to both electrodes.

To date, rapid progress has been made on each isolated layer, with major emphasis on perovskite film processing and relevant material design. As a result, various processing approaches have been reported that focus on the absorber properties and consequent device performance (7–15). These include one-step and sequential solution deposition (7–10), vacuum deposition (11), and vapor-assisted solution processing (12), which clearly show a strong relation between the structure, composition, and corresponding properties of the perovskite absorber. Based on a deep understanding of its hybrid nature, a delicate control over the carrier behavior in the perovskite film is expected. Despite our comparatively nascent understanding of this class of absorber

¹Department of Materials Science and Engineering, University of California, Los Angeles, CA 90095, USA. ²California NanoSystems Institute, University of California, Los Angeles, CA 90095, USA.

*These authors contributed equally to this work. †Corresponding author. E-mail: yangy@ucla.edu